RSC Advances

PAPER

View Article Online
View Journal | View Issue

Cite this: *RSC Adv.*, 2022, **12**, 19384

Effect of Pr/Zn on the anti-humidity and acetone-sensing properties of Co_3O_4 prepared by electrospray†

Xiangxiang Fan, ‡*[ab] Junfeng Wang,‡[a] Chuanlong Sun,[a] Chun Huang,[ab] Yujie Lu,[ab] Pan Dai,[ab] Yajuan Xu[a] and Wuming He[ab]

Received 27th May 2022
Accepted 28th June 2022

DOI: 10.1039/d2ra03321f

rsc.li/rsc-advances

Co_3O_4 is a P-type metal-oxide semiconductor which can realize acetone detection at a lower temperature, but the lower working temperature brings the enhanced humidity effect. In order to solve the problem of a Co_3O_4 gas sensor being easily affected by humidity, an acetone-sensing material of Co_3O_4 mixed with Pr/Zn was prepared by electrospray in this work. The optimal working temperature of Pr/Zn–Co_3O_4 is 160 °C, and the detection limit can reach 1 ppm. The fluctuation of the acetone response is about 7.7% in the relative humidity range of 30–90%. Compared with pure Co_3O_4, the anti-humidity property of this material is obviously enhanced, but the gas-sensing response deteriorates. Compared with Pr–Co_3O_4, the anti-humidity and acetone sensing properties of Pr/Zn–Co_3O_4 were both improved. The morphology, composition, crystal state and energy state of the material were analyzed by SEM, EDS, XRD and XPS. The material of Pr/Zn–Co_3O_4 is a multi-component mixed material composed of $PrCoO_3$, ZnO, Pr_6O_{11} and Co_3O_4. The improved anti-humidity and acetone sensing properties exhibited by this material are the result of the synergistic effect of ZnO and Pr^{3+}.

1. Introduction

Acetone is an important respiratory marker of diabetes. The accurate and stable detection of acetone in breathing gas is of great significance to changing the existing medical diagnosis model for diabetes. As a low-cost and easy-to-manufacture gas sensor, the metal oxide sensor has been widely used in research of acetone detection.[1–5] However, the main problems currently faced in practical application are the low concentration of markers and high humidity in the breathing gas, which requires the sensor to have a lower detection limit and better anti-humidity properties.

Co_3O_4 is a p-type metal-oxide semiconductor, which was widely used in the detection of acetone due to catalytic activity for volatile organic compounds (VOCs) and lower working temperature.[6–10] Su *et al.* prepared flower-shaped Co_3O_4, and the detection limit of acetone reached 0.2 ppm.[6] Qiao *et al.* prepared 3D radial Co_3O_4 nanorod clusters, and the detection limit of acetone reached 0.1 ppm.[7] Because the acetone concentration in breathing gas is more than 0.3–0.9 ppm, Co_3O_4 is a promising material for acetone sensors for breathing gas. The acetone sensitivity of Co_3O_4 can be further improved by constructing composed materials.[11–14] The composed materials of Co_3O_4 nanorod and ZnO nanosheet prepared by Jang *et al.* responded to 5 ppm acetone as high as 29, and the theoretical detection limit could reach 5 ppb.[15] However, the sensitivity and stability of Co_3O_4 for acetone sensing deteriorate in a high-humidity environment.[16–18] Srinivasan *et al.* have shown that high humidity conditions could affect the acetone sensitivity of Co_3O_4, and the acetone response dropped by 16.59% under a relative humidity of 89%.[16] Zhou *et al.* found that the increase of relative humidity would also reduce the long-term stability of the Co_3O_4 acetone sensor, where the sensor response dropped by 10% in 20 days under a relative humidity of 33%.[17] Therefore, humidity is a negative factor restricting the application of Co_3O_4 for respiration detection, but there are still few reports on the research that actually proposes to solve the influence of humidity on the Co_3O_4 acetone sensor.

Doping is a commonly used strategy to improve the performance of metal oxide gas sensors.[19,20] The elements of Ce, Tb and Pr all have two valence states of 3+ and 4+. Because of the valence states, Ce, Tb and Pr all have reversible oxidation–reduction reactions, which can remove hydroxyl groups and promote the formation of ionized oxygen. These elements have been doped into the sensing materials to realize the anti-humidity property of the gas sensors.[21–24] Yoon *et al.* used layer-by-layer coating to modify CeO_2 nanoclusters on the surface of In_2O_3 hollow spheres, which exhibited humidity

---

[a] *School of Information Engineering, Huzhou University, Huzhou 313000, China. E-mail: fanxiangxiang@zjhu.edu.cn*

[b] *Zhejiang Province Key Laboratory of Smart Management & Application of Modern Agricultural Resources, Huzhou University, Huzhou 313000, China*

† Electronic supplementary information (ESI) available. See https://doi.org/10.1039/d2ra03321f

‡ The authors contribute equally to this work.

independence.[21] Kwak *et al.* prepared Tb-doped SnO_2 yolk–shell spheres by ultrasonic spray pyrolysis, which exhibited similar gas responses in dry condition and relative humidity of 80%.[22] The Pr-doped In_2O_3 prepared by Kim *et al.* also exhibited similar gas responses in different humid conditions.[23] It can be seen that doping of Ce, Tb and Pr provide a new way for the development of gas sensors with anti-humidity property. However, these sensors all worked at a high temperature of 450 °C, and the higher operating temperature promotes the humidity independence of the sensor. In addition, although the doping of Ce, Tb and Pr improved the humidity independence, the gas responses of the sensors reduced to a greater extent. The anti-humidity performance of a sensor with the doping of Ce, Tb and Pr at a low operating temperature and the method to enhance sensitivity of the sensor with the doping of Ce, Tb and Pr still need to be further investigated.

In this work, multi-element hybrid material of Co_3O_4 and the element of Pr/Zn was prepared by electrospray. This work tried to synergize the reversible redox reaction characteristics of Pr and the n-type semiconductor characteristics of ZnO to achieve anti-humidity and acetone enhanced-sensing properties. The mechanism of anti-humidity and enhanced-sensing was initially investigated through the characterization and analysis of the hybrid material.

2. Experimental

2.1 Preparation of materials

Firstly, the electrospray solution was prepared. The solvent was made up of ethanol and water in a ratio of 1 : 1. *A* mmol of cobalt acetate tetrahydrate ($Co(CH_3COO)_2 \cdot 4H_2O$, AR), *B* mmol of praseodymium nitrate hexahydrate ($Pr(NO_3)_3 \cdot 6H_2O$, AR) and *C* mmol of zinc acetate dihydrate ($Zn(CH_3COO)_2 \cdot 2H_2O$, AR) were dissolved in 10 mL of the above mixed solvent and fully stirred with a magnetic stirrer to obtain a uniform solution. Next, the configured solution was transferred into a syringe for electrospray. The schematic diagram of electrospray system has been shown in our previous report.[25] The liquid supply flow of the syringe pump was 0.6 mL h^{-1}. The voltage and distance between the nozzle and the collector were 8 kV and 7 cm respectively. The collector was kept at the temperature of 200 °C. Finally, the precursor materials were calcined. The calcination process was carried out in a muffle furnace with a calcination temperature of 600 °C for 3 h. The heating rate of the muffle furnace was set as 2 °C min^{-1}. All materials were used in the purchased state without any pretreatment.

According to the above process, seven samples with different parameters were prepared, and the parameters are shown in Table 1.

Table 1 The composition parameters of the solutes in the samples

Samples	*A*	*B*	*C*
Co_{100}	2	0	0
Pr_5Co_{95}	1.9	0.1	0
$Pr_{10}Co_{90}$	1.8	0.2	0
$Pr_{20}Co_{80}$	1.6	0.4	0
$Pr_{10}Zn_{10}Co_{80}$	1.6	0.2	0.2
$Pr_{10}Zn_{20}Co_{70}$	1.4	0.2	0.4
$Pr_{10}Zn_{40}Co_{50}$	1	0.2	0.8

2.2 Characterization of materials

The morphology and element composition of the samples were analyzed by scanning electron microscope and energy dispersive X-ray spectroscopy (SEM and EDS, SU8010, Hitachi, Japan). X-ray diffraction spectroscopy (XRD, Ultima IV, Rigaku) was used to analyze the crystal composition and crystal quality of the samples. X-ray photoelectron spectroscopy (XPS, Escalab Xi+, Thermo Fisher Scientific) was used to analyze the chemical state of the Pr, Co, Zn and O elements in the sample.

2.3 Gas sensing measurement

In order to detect the acetone responses of all the samples in different humidity environments, a test system was built as shown in Fig. 1. The test system was consisted of an air pump, a filter, a saturated salt solution and a test chamber. The size of the test chamber in this work was 300 mm × 300 mm × 200 mm with the volume of 18 L. The air was passed into the filter through the air pump to filter out the macromolecular substances and the water molecules in the air. Then the gas was passed into the saturated salt solution to generate the air with the required humidity. Finally, the air was passed into the test chamber. The final humidity in the test chamber was calibrated by a humidity sensor, and the relative humidity in the test chamber could be adjusted between 30% and 90%.

During gas sensing test, the saturated acetone steam was injected into the test chamber to obtain the corresponding concentration of acetone test gas. The volume of saturated acetone steam injected into the test chamber could be calculated according to our previous report.[26] The formula for calculating the volume of saturated acetone vapor was $V_g = P_0 \cdot C_g \cdot V_c / P_g$, where P_0 is the ambient atmospheric pressure, C_g is the required concentration of acetone, V_c is the volume of the test chamber, and P_g is the saturated vapor pressure of acetone. After the gas sensing test was complete, the acetone-containing gas was removed from the test chamber and replaced with fresh air.

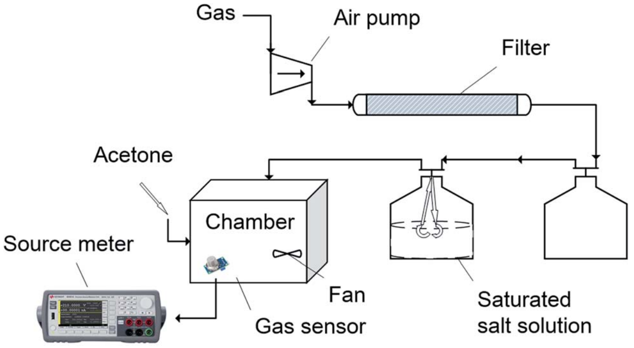

Fig. 1 Schematic diagram of gas sensing test system.

The resistance of the sensor was measured and saved by the source meter (B2902A, Keysight). The response was defined as $(R_g - R_a)/R_a$, where R_g and R_a is the resistance of the sensor in acetone atmosphere and in air respectively. The response and recovery time was defined as the time required for the resistance to change to 90% of the change amplitude.

3. Results and discussion

3.1 Gas sensing properties

Fig. 2(a) shows the responses variation of Co_{100}, Pr_5Co_{95}, $Pr_{10}Co_{90}$ and $Pr_{20}Co_{80}$ with temperature. The responses of the four samples all show a trend of first becoming larger and then smaller as the temperature increases. Among them, the optimal working temperature of Co_{100} is 190 °C, and the optimal working temperature of the hybrid samples with Pr reduced to 160 °C. Fig. 2(b) shows the responses comparison of the four samples to 50 ppm acetone at the optimal working temperature. The response of Co_{100} is the largest, and the responses of the hybrid samples with Pr are greatly weakened. The response of Pr_5Co_{95} is only 0.56, which is only a quarter of Co_{100}. With the Pr concentration further increase, the response of the samples is further reduced, but the change is not significant. It can be seen that the addition of Pr will reduce the sensitivity of sensing materials.

Fig. 2(c) shows the responses variation of Co_{100}, Pr_5Co_{95}, $Pr_{10}Co_{90}$ and $Pr_{20}Co_{80}$ with relative humidity. During the relative humidity increases from 30% to 90%, the responses of all the samples decrease. But, the response of Co_{100} is still larger than those of the hybrid samples in different relative humidity. Fig. 2(d) shows the responses ratios of the four samples at 90% and 30% relative humidity. As figure shown, the ratio of $Pr_{10}Co_{90}$ is the largest. Compared with the response in 30% relative humidity, the response in 90% relative humidity only drops by 9%. The ratio of Co_{100} is the smallest. Compared with the response in 30% relative humidity, the response of Co_{100} in 90% relative humidity drops by 28%. It can be seen that the suitable incorporation of Pr can greatly improve anti-humidity property of Co_3O_4.

Fig. 3(a) shows the responses variation of $Pr_{10}Co_{90}$, $Pr_{10}Zn_{10}Co_{80}$, $Pr_{10}Zn_{20}Co_{70}$ and $Pr_{10}Zn_{40}Co_{50}$ with temperature. The responses of the four samples have the same trend with temperature increases, and the largest responses of the samples are achieved at 160 °C. As shown in Fig. 3(b), the incorporation of Zn can enhance the response of $Pr_{10}Co_{90}$. The response of $Pr_{10}Zn_{40}Co_{50}$ to 50 ppm acetone is 0.93, which is about twice that of $Pr_{10}Co_{90}$. Fig. 3(c) shows the responses variation of $Pr_{10}Co_{90}$, $Pr_{10}Zn_{10}Co_{80}$, $Pr_{10}Zn_{20}Co_{70}$ and $Pr_{10}Zn_{40}Co_{50}$ with relative humidity. In the range of 30–90% relative humidity, the responses of the four samples maintain good stability. As

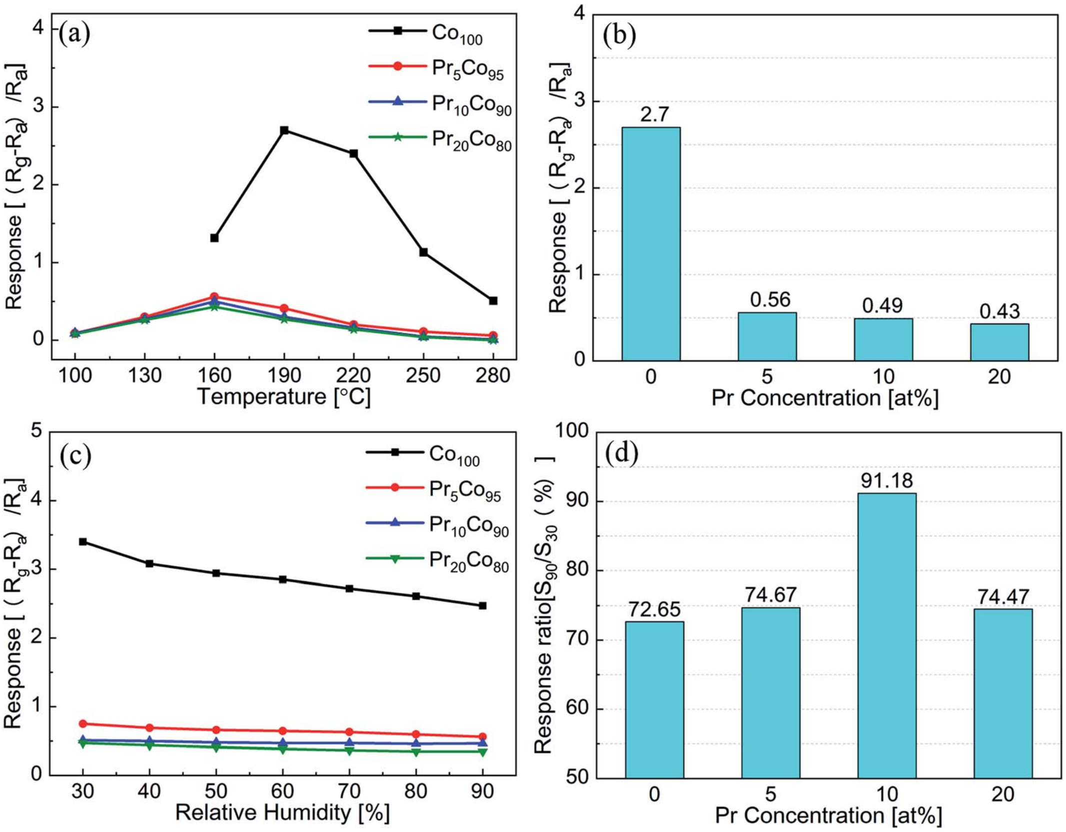

Fig. 2 Responses to 50 ppm acetone at (a) different temperature and (b) the optimal working temperature for Co_{100}, Pr_5Co_{95}, $Pr_{10}Co_{90}$ and $Pr_{20}Co_{80}$. (c) Responses to 50 ppm acetone in different relative humidity, and (d) ratios of responses at 90% and 30% relative humidity for Co_{100}, Pr_5Co_{95}, $Pr_{10}Co_{90}$ and $Pr_{20}Co_{80}$.

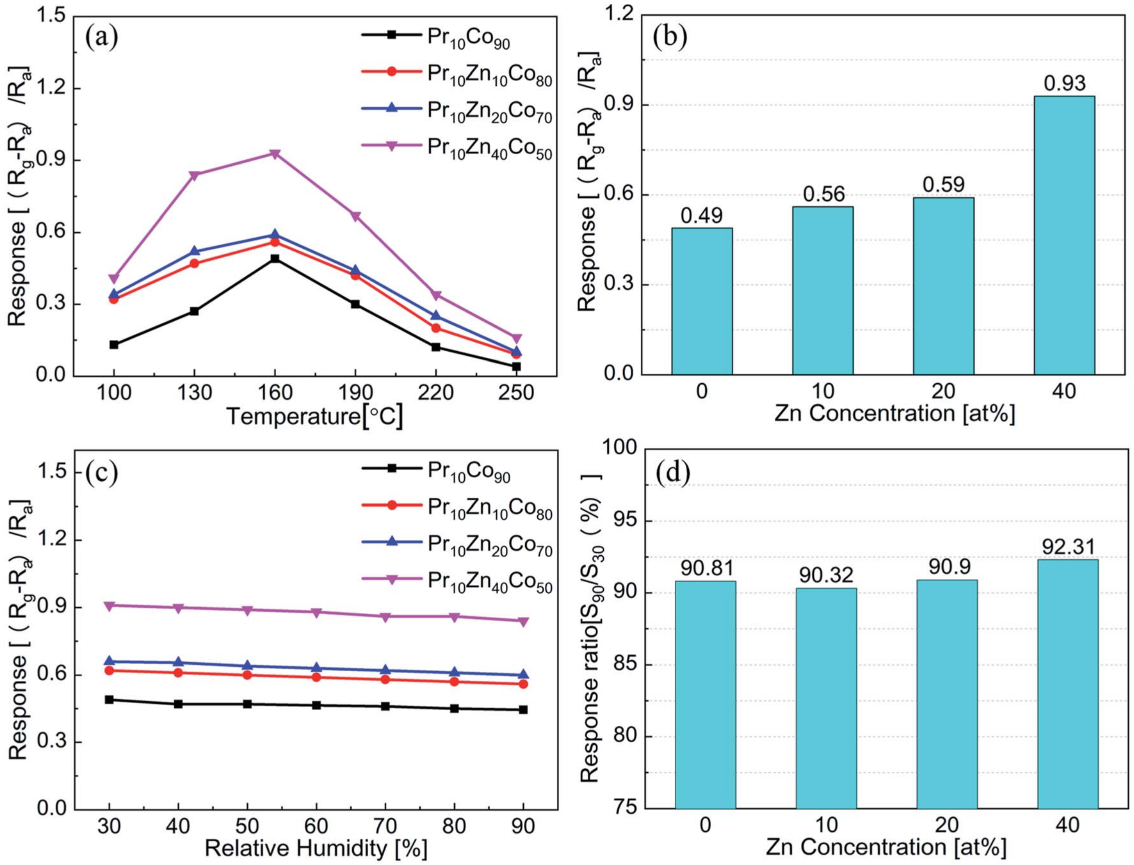

Fig. 3 Responses to 50 ppm acetone at (a) different temperature and (b) the optimal working temperature for $Pr_{10}Co_{90}$, $Pr_{10}Zn_{10}Co_{80}$, $Pr_{10}Zn_{20}Co_{70}$ and $Pr_{10}Zn_{40}Co_{50}$. (c) Responses to 50 ppm acetone at different relative humidity, and (d) ratios of responses in 90% and 30% relative humidity for $Pr_{10}Co_{90}$, $Pr_{10}Zn_{10}Co_{80}$, $Pr_{10}Zn_{20}Co_{70}$ and $Pr_{10}Zn_{40}Co_{50}$.

Fig. 3(d) shown, the ratios of the four samples at 90% and 30% relative humidity are all greater than 90%. Among them, the response of $Pr_{10}Zn_{40}Co_{50}$ in 90% relative humidity is only 7.7% lower than that in 30% relative humidity. This indicates that the incorporation of Zn could enhance the acetone sensitivity of Pr–Co_3O_4 and maintain a good anti-humidity property.

Fig. 4(a) shows the comparison of the anti-humidity and acetone sensing properties of Co_{100}, $Pr_{10}Co_{90}$ and $Pr_{10}Zn_{40}Co_{50}$. Co_{100} exhibits the largest gas sensing response, but poor anti-humidity property. $Pr_{10}Co_{90}$ exhibits better anti-humidity property, but the gas sensing response is greatly deteriorated. $Pr_{10}Zn_{40}Co_{50}$ maintains excellent anti-humidity property while shows a good gas sensing property. It indicates that the multiple incorporation of Pr and Zn into Co_3O_4 can synergistically improve the anti-humidity and acetone sensing properties.

Fig. 4(b) shows the responses of $Pr_{10}Zn_{40}Co_{50}$ to different concentrations of acetone. The sample shows a good response–recovery to 1–50 ppm acetone, and the response to 1 ppm acetone is 0.14. Fig. 4(c) shows the response–recovery curve of $Pr_{10}Zn_{40}Co_{50}$ to 50 ppm acetone. The response and recovery time of the sensor is 70 and 330 s, respectively. Fig. 4(d) shows the responses comparison of $Pr_{10}Zn_{40}Co_{50}$ to 50 ppm acetone, ethanol, triethylamine, methanol, benzene, SO_2, CO and NO_2. Among them, the response to acetone is the highest.

Fig. 5(a) shows the cycle test of $Pr_{10}Zn_{40}Co_{50}$ to 50 ppm acetone. The response curves of the sample maintain a good consistency during the four-cycle tests. Fig. 5(b) shows the response curves of $Pr_{10}Zn_{40}Co_{50}$ to 50 ppm acetone over two weeks. The sensor shows good stability with a relative standard deviation of 3.08% for the response values.

The anti-humidity comparison of Co_3O_4-based acetone sensor between this work and the previous reported work is listed in Table 2. All the sensors in the references show high acetone responses under low humidity conditions. However, under high humidity conditions greater than 80%, the acetone responses of the sensors show a drop of more than 15%, and some even drop by 66.7%.[16–18,27–29] The sensor of $Pr_{10}Zn_{40}Co_{50}$ in this work shows good agreement in low and high humidity, and the relative deviation is much smaller than the reported.

3.2 Materials characterization

Fig. 6 shows the SEM images and EDS spectra of Co_{100}, $Pr_{10}Co_{90}$ and $Pr_{10}Zn_{40}Co_{50}$. As SEM images shown, all three samples are composed of nanoparticles, which include bottom and surface layer. The bottom is the particle layer and the surface is dispersed with aggregated particle clusters. Among them, Co_{100} has a higher agglomeration density and a rougher surface, while $Pr_{10}Zn_{40}Co_{50}$ has a flatter surface with smaller and more

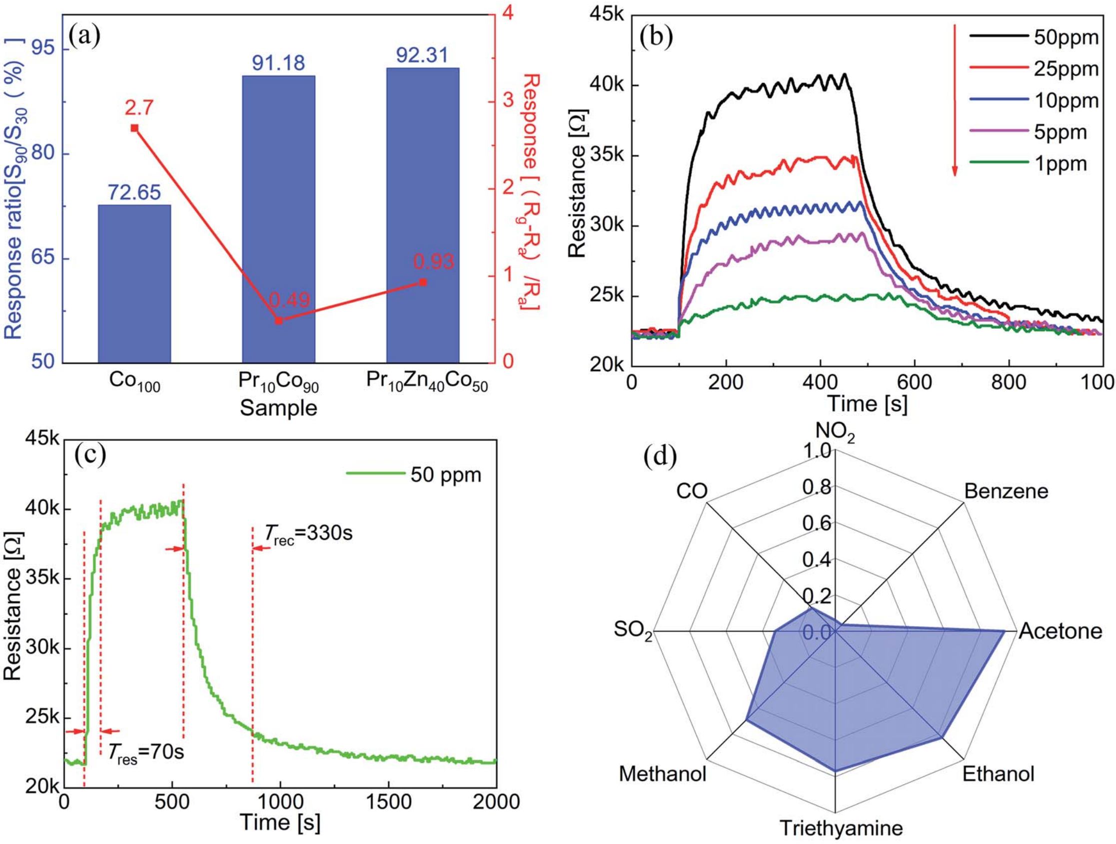

Fig. 4 (a) Responses to 50 ppm acetone and ratios of response at 90% and 30% relative humidity for Co_{100}, $Pr_{10}Co_{90}$ and $Pr_{10}Zn_{40}Co_{50}$. (b) Response–recovery curves to different concentrations of acetone. (c) Response–recovery curves to 50 ppm acetone. (d) Response to 50 ppm acetone and other gases.

dispersed clusters. The elementals proportions of Co, Pr and Zn in the samples were analyzed by EDS. The molar proportion of Co element in Co_{100} is 100%. The molar proportions of Co and Pr in $Pr_{10}Co_{90}$ are approximately 91% and 9%, respectively. The molar proportions of Co, Pr and Zn in $Pr_{10}Zn_{40}Co_{50}$ are approximately 50%, 9% and 41%, respectively. The molar proportions of the elements are almost the same as the experimental design.

Fig. 7 shows the XRD spectra of Co_{100}, $Pr_{10}Co_{90}$ and $Pr_{10}Zn_{40}Co_{50}$. The diffraction peaks of Co_{100} are located at 31.28°, 36.86°, 36.58°, 44.8°, 55.62°, 59.38° and 65.24°, corresponding to [2 2 0], [3 1 1], [2 2 2], [4 0 0], [4 2 2], [5 1 1] and [4 4 0] crystal planes of spinel Co_3O_4 (JCPDS 43-1003). As the spectra shows that Co_{100} is composed of Co_3O_4 without other impurities. In addition to the diffraction peaks of Co_3O_4, $Pr_{10}Co_{90}$ has three new diffraction peaks located at 33.3°, 41.26° and 47.9°, respectively. These three peaks correspond to [2 2 0], [2 2 2] and

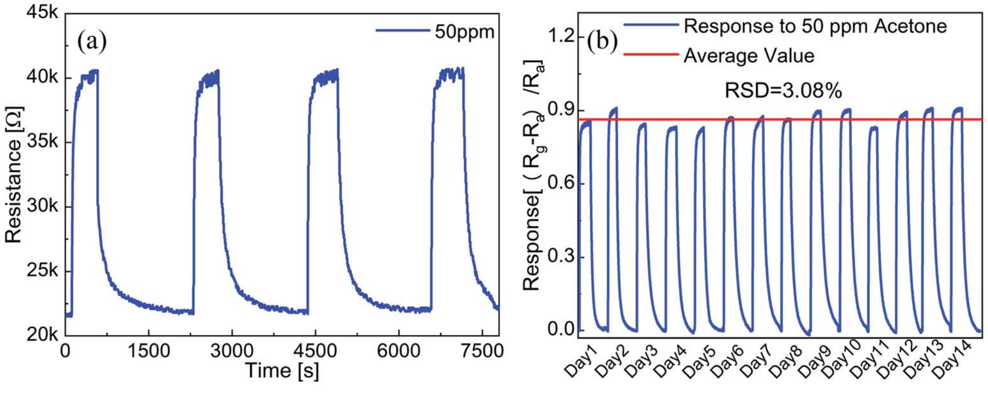

Fig. 5 (a) Cycle tests curves to 50 ppm acetone for $Pr_{10}Zn_{40}Co_{50}$. (b) Responses to 50 ppm acetone over two weeks.

Table 2 Comparison of anti-humidity between this work and the reported works[a]

Materials	Temp. (°C)	Con. (ppm)	Res./low hum. (%)	Res./high hum. (%)	Relative deviation (%)	Ref.
Co_3O_4	500	50	242/32	195/89	19.4	16
Co_3O_4	240	500	3.16/33	~1.3/~95	58.9	17
Co_3O_4	150	100	34.2/30	15.3/80	55.3	27
Co_3O_4/graphene	190	1	54.3/30	45.6/90	16	18
Co_3O_4/graphene	160	50	5.4/20	4/90	25.9	28
Pt–Co_3O_4	200	0.5	2.1/0	0.7/80	66.7	29
Pr/Zn–Co_3O_4	160	50	0.91/30	0.84/90	7.7	This work

[a] Res. was defined as $(R_g - R_a)/R_a$. Relative deviation was defined as (Res(low) − Res(high))/Res(low). Temp.: temperature; Con.: concentration; res.: response; hum.: humidity; ref.: reference.

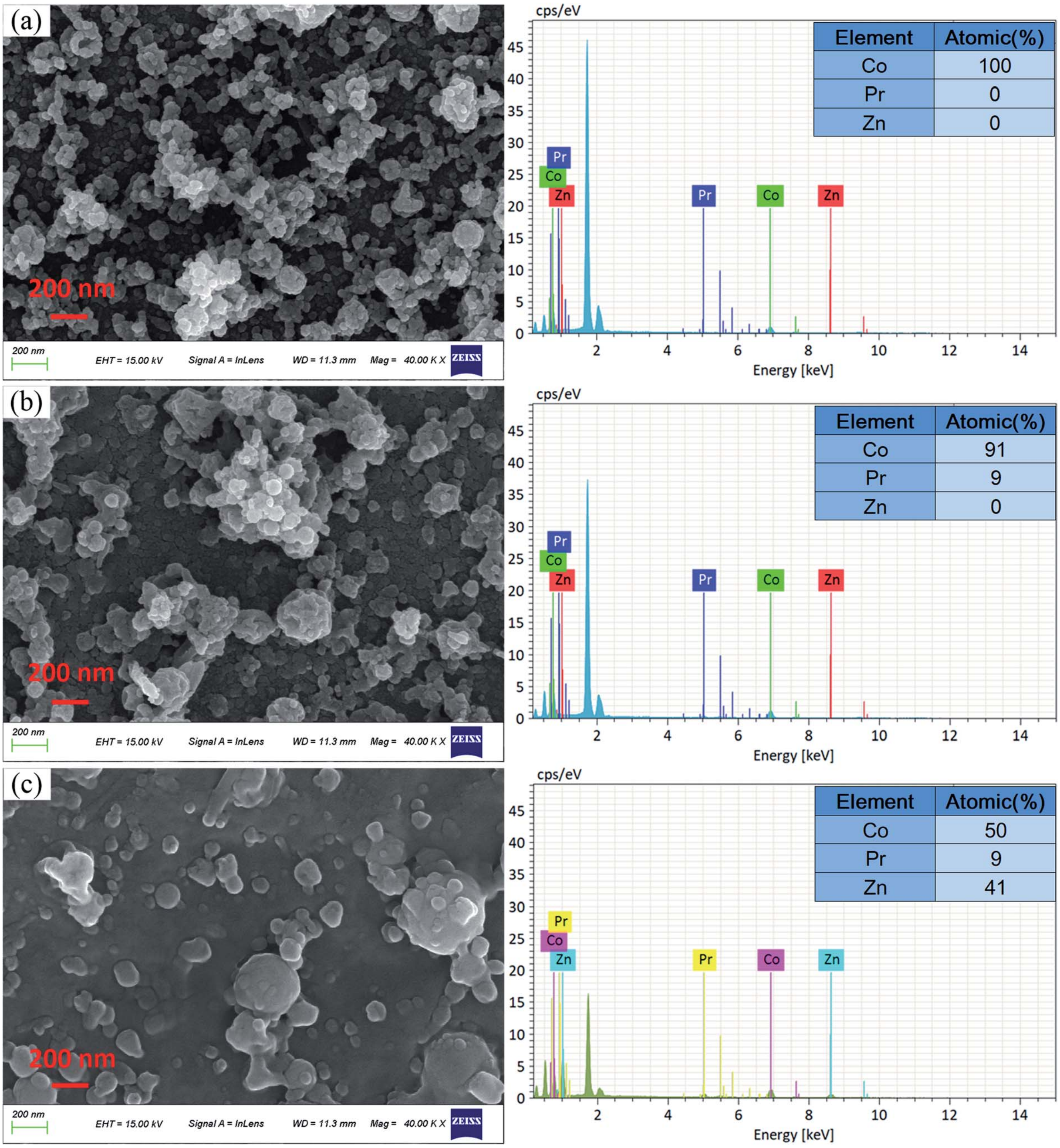

Element	Atomic(%)
Co	100
Pr	0
Zn	0

Element	Atomic(%)
Co	91
Pr	9
Zn	0

Element	Atomic(%)
Co	50
Pr	9
Zn	41

Fig. 6 SEM images and EDS spectra of (a) Co_{100}, (b) $Pr_{10}Co_{90}$ and (c) $Pr_{10}Zn_{40}Co_{50}$.

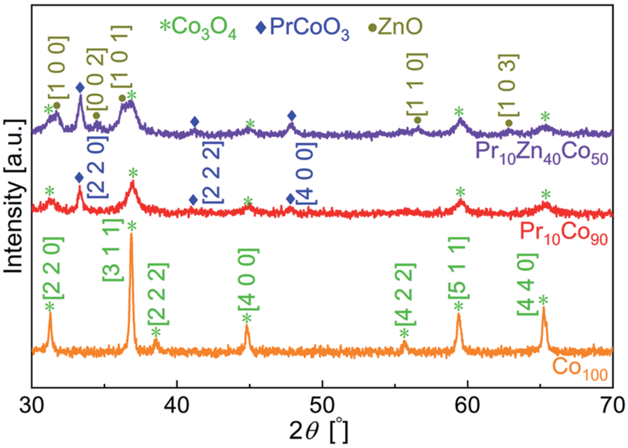

Fig. 7 XRD spectra of (a) Co_{100}, (b) $Pr_{10}Co_{90}$ and (c) $Pr_{10}Zn_{40}Co_{50}$.

[4 0 0] crystal planes of $PrCoO_3$ (JCPDS 25-1069), which indicate that $Pr_{10}Co_{90}$ is a hybrid material of Co_3O_4 and $PrCoO_3$. For $Pr_{10}Zn_{40}Co_{50}$, the other five new diffraction peaks appear on the spectrum, which are located at 31.7°, 34.4°, 36.24, 56.62° and 62.8°. These five peaks correspond to [1 0 0], [0 0 2], [1 0 1], [1 1 0] and [1 0 3] crystal planes of ZnO (JCPDS 36-1451). This indicates that $Pr_{10}Zn_{40}Co_{50}$ contains at least three kinds of crystals including Co_3O_4, $PrCoO_3$ and ZnO.

Fig. 8(a)–(c) show the high-resolution XPS spectra of Co 2p in Co_{100}, $Pr_{10}Co_{90}$ and $Pr_{10}Zn_{40}Co_{50}$. The peak near 794.7 eV corresponds to Co $2p_{1/2}$, which can be divided into the peaks of 795.9 eV and 794.6 eV by Gaussian fitting. The peak near 779.7 eV corresponds to Co $2p_{3/2}$, which can be divided into the peaks of 780.5 eV and 779.5 eV. Among these peaks, the fitting peaks of 795.9 eV and 780.5 eV are derived from Co^{2+}, while the fitting peaks of 794.6 eV and 779.5 eV are derived from Co^{3+}. By analyzing the peak areas, the ratios of the Co^{2+} and Co^{3+} in the three samples of Co_{100}, $Pr_{10}Co_{90}$ and $Pr_{10}Zn_{40}Co_{50}$ are

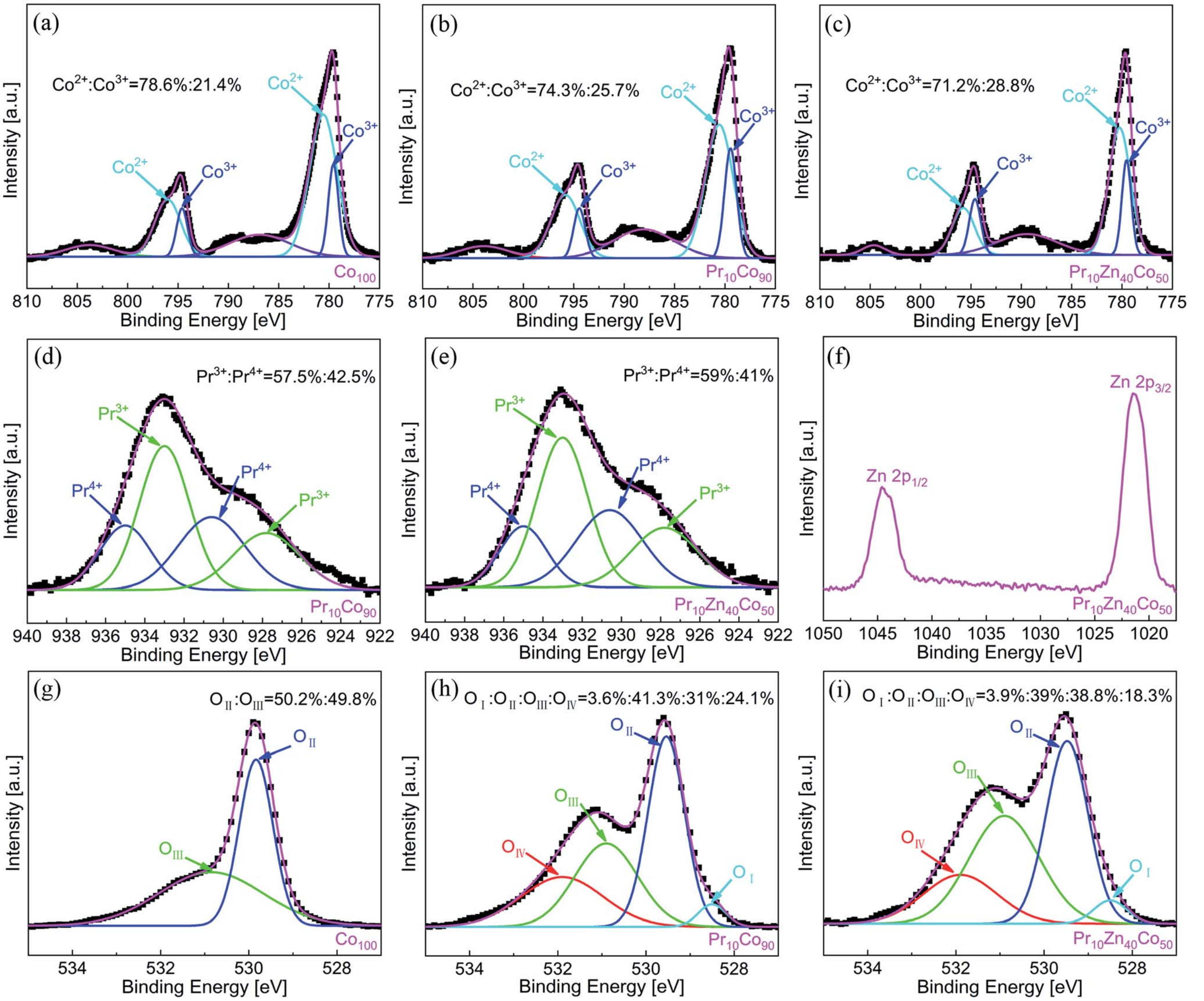

Fig. 8 High-resolution XPS spectra of (a and g) Co_{100}, (b, d and h) $Pr_{10}Co_{90}$ and (c, e, f and i) $Pr_{10}Zn_{40}Co_{50}$.

78.6 : 21.4, 74.3 : 25.7 and 71.2 : 28.8, respectively. Due to the incorporation of Pr, the proportion of Co^{3+} in the hybrid material increases, which is attributed to the formation of $PrCoO_3$.

Fig. 8(d) and (e) show the high-resolution XPS spectra of Pr $3d_{5/2}$ in $Pr_{10}Co_{90}$ and $Pr_{10}Zn_{40}Co_{50}$. This peak is located near 933 eV, and can be divided into the peaks of 935 eV, 933 eV, 930.6 eV and 927.8 eV. The fitting peaks of 935 eV and 930.6 eV are derived from Pr^{4+}, while the fitting peaks of 933 eV and 927.8 eV are derived from Pr^{3+}. By analyzing the area of the peaks, the ratios of the peaks area of Pr^{3+} and Pr^{4+} are 57.5 : 42.5 and 59 : 41 for $Pr_{10}Co_{90}$ and $Pr_{10}Zn_{40}Co_{50}$, respectively. The proportions of Pr^{3+} and Pr^{4+} in the hybrid samples are consistent with that in Pr_6O_{11} reported in the previous literature.[23] It indicates that the samples of $Pr_{10}Co_{90}$ and $Pr_{10}Zn_{40}Co_{50}$ also contain Pr_6O_{11}.

Fig. 8(f) shows the high-resolution XPS spectrum of Zn in $Pr_{10}Zn_{40}Co_{50}$. The peak near 1044.6 eV is derived from Zn $2p_{1/2}$, and the peak near 1021.5 eV is derived from Zn $2p_{3/2}$.

Fig. 8(g)–(i) show the high-resolution XPS spectra of O 1s in Co_{100}, $Pr_{10}Co_{90}$ and $Pr_{10}Zn_{40}Co_{50}$. The O 1s peaks of the three samples can be divided into 4 peaks, which are located at 531.9 eV (O_{IV}), 530.9 eV (O_{III}), 529.5 eV (O_{II}) and 528.5 eV (O_I). O_I, O_{II}, O_{III} and O_{IV} are derived from Pr^{3+}–O, crystal lattice oxygen, adsorbed oxygen and Pr^{4+}–O. The proportions of different oxygen components are analyzed based on the area ratio. Since Co_{100} does not contain Pr, its spectrum only contains O_{II} and O_{III}, and the components proportions are 50.2% and 49.8%. The proportions of O_I, O_{II}, O_{III} and O_{IV} in $Pr_{10}Co_{90}$ are 3.6%, 41.3%, 31% and 24.1%, while the proportions of O_I, O_{II}, O_{III} and O_{IV} in $Pr_{10}Zn_{40}Co_{50}$ are 3.9%, 39%, 38.8% and 18.3%. Among the oxygen components, O_{III} is the key to the gas sensitivity. In the three samples, Co_{100} has the highest proportion of O_{III}, while $Pr_{10}Co_{90}$ has the lowest proportion.

3.3 Gas sensing mechanism

According to the response curves in Fig. S1,† the samples of Co_{100}, $Pr_{10}Co_{90}$ and $Pr_{10}Zn_{40}Co_{50}$ all exhibit the characteristics of p-type semiconductor. For p-type semiconductor, the gas sensitivity depends on the thickness of the hole accumulation layer on the surface. Due to the chemical adsorption of oxygen, oxygen traps electrons from the sensing material to form oxygen ions when a sample is exposed to the air, so that the hole accumulation layer on the surface will increase and the resistance will decrease. When the sample is exposed to acetone, oxygen ions react with acetone and release electrons back to the sensing material, resulting in a reduction of the hole accumulation layer and an increase of resistance. The process can be expressed by the following reactions:[30]

$$O_2(ads) + e^- \rightarrow O_2^-(ads)$$

$$O_2^-(ads) + e^- \rightarrow 2O^-(ads)$$

$$CH_3COCH_3(g) + 8O^-(ads) \rightarrow 3CO_2 + 3H_2O + 8e^-$$

$$CH_3COCH_3(g) + 4O_2^-(ads) \rightarrow 3CO_2 + 3H_2O + 4e^-$$

Since the working temperatures of the sensors are relatively low, water molecules will adsorb on the surface and react with the adsorbed oxygen ions to form hydroxyl groups and electronics in a high-humidity environment, resulting in water poisoning of the sensing material and reducing of gas sensitivity. Because Pr has reversible oxidation–reduction reaction property, Pr^{3+} can promote the reverse reaction process of water poisoning. The hydroxyl groups could be effectively removed and the oxygen ions are regenerated with the transition from Pr^{3+} to Pr^{4+}. Pr^{4+} recaptures the electrons brought by the water molecule reaction and turns into Pr^{3+}. During the above cyclic redox reaction, the reactants and products are equal. When the hydroxyl groups on the materials surface are completely removed, the resistance and response of the sensitive material are hardly affected. Therefore, $Pr_{10}Co_{90}$ and $Pr_{10}Zn_{40}Co_{50}$ shows better consistency of gas responses than Co_{100} in different relative humidity. The process can be expressed by the following reactions:[23]

$$H_2O + O^- \leftrightarrow 2OH + e^-$$

$$Pr^{3+} + 2OH \rightarrow Pr^{4+} + H_2O + O^-(ads)$$

$$Pr^{4+} + e^- \rightarrow Pr^{3+}$$

The gas sensitivity of Co_{100}, $Pr_{10}Co_{90}$ and $Pr_{10}Zn_{40}Co_{50}$ mainly depend on the surface reaction. Co_3O_4 contains two kinds of Co ions (Co^{2+} and Co^{3+}), in which Co^{2+} is the reaction sites.[31] Therefore, the concentration of Co^{2+} on surface will affect the surface reaction. From XPS analysis, it can be found that the concentration of Co^{2+} on surface of the hybrid samples is reduced because of the formation of $PrCoO_3$, which results in

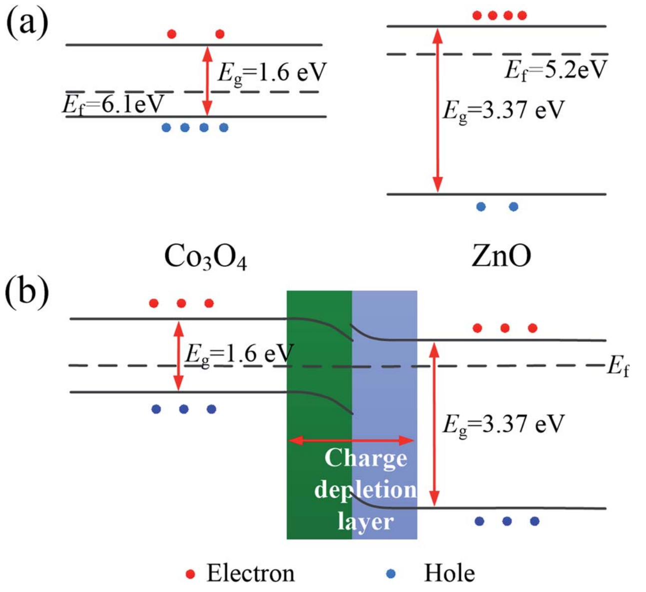

Fig. 9 Band structures of (a) Co_3O_4 and ZnO and (b) Co_3O_4–ZnO heterojunction.

a reduction of reaction sites and a decrease of the sensitivity. Although the Co^{2+} concentration of $Pr_{10}Zn_{40}Co_{50}$ is also reduced, the gas sensitivity is improved because of the addition of ZnO. The enhanced sensitivity could be contributed to two reasons. First, ZnO in the hybrid sample brings more electrons, which promotes the increase of oxygen ions adsorbed on the surface. This can be confirmed from the XPS diagram. The concentration of adsorbed oxygen on the surface of $Pr_{10}Zn_{40}Co_{50}$ is relatively higher than that of $Pr_{10}Co_{90}$. Second, p–n heterojunctions are formed in $Pr_{10}Zn_{40}Co_{50}$. As shown in Fig. 9(a), the Fermi level of Co_3O_4 is located at 6.1 eV, while that of ZnO is at 5.2 eV. When the two metal oxides are in contact, ZnO transfers electrons to Co_3O_4 in order to maintain the unity of the Fermi level at the interface. Therefore, the p–n heterojunction is formed with the appearance of a charge depletion layer at the interface, as shown in Fig. 9(b). Heterojunction can adjust the barrier of the material, causing a greater change of resistance during the gas reaction.[32,33]

4. Conclusions

An acetone sensing material of $Pr_{10}Zn_{40}Co_{50}$ was prepared in this work, which is a hybrid material of $PrCoO_3$, ZnO, Pr_6O_{11} and Co_3O_4. Compared with pure Co_3O_4, the optimal working temperature of $Pr_{10}Zn_{40}Co_{50}$ decreases, and the hybrid material exhibits more stable responses to acetone in different humidity conditions. The detection limit for acetone could reach 1 ppm. The anti-humidity property of $Pr_{10}Zn_{40}Co_{50}$ result from the reverse reaction of Pr to water poisoning, which weakens the reaction of water molecules on the surface of the material to generate hydroxyl groups. Compared with $Pr_{10}Co_{90}$ containing only Pr addition, the sensitivity of $Pr_{10}Zn_{40}Co_{50}$ is also enhanced, which depends on the increase of adsorbed oxygen on the surface and the adjustment of the potential barrier by the p–n heterojunction. This work shows that synergistic effects of each material in hybrid material can improve the gas sensing properties.

Conflicts of interest

There are no conflicts to declare.

Acknowledgements

This work was supported by Zhejiang Provincial Natural Science Foundation (LQ20F010001).

References

1 J. Cao, N. Zhang, S. Wang, C. Chen and H. Zhang, Researching the crystal phase effect on gas sensing performance in In_2O_3 nanofibers, *Sens. Actuators, B*, 2020, **305**, 127475.

2 H.-J. Cho, S.-J. Choi, N.-H. Kim and I.-D. Kim, Porosity controlled 3D SnO_2 spheres *via* electrostatic spray: selective acetone sensors, *Sens. Actuators, B*, 2020, **304**, 127350.

3 P. Wang, T. Dong, C. Jia and P. Yang, Ultraselective acetone-gas sensor based ZnO flowers functionalized by Au nanoparticle loading on certain facet, *Sens. Actuators, B*, 2019, **288**, 1–11.

4 N. Chen, Y. Li, D. Deng, X. Liu, X. Xing, X. Xiao and Y. Wang, Acetone sensing performances based on nanoporous TiO_2 synthesized by a facile hydrothermal method, *Sens. Actuators, B*, 2017, **238**, 491–500.

5 D. Han, Y. Ji, F. Gu and Z. Wang, Cobalt oxide nanorods with special pore structure for enhanced ethanol sensing performance, *J. Colloid Interface Sci.*, 2018, **531**, 320–330.

6 C. Su, L. Zhang, Y. Han, X. Chen, S. Wang, M. Zeng, N. Hu, Y. Su, Z. Zhou, H. Wei and Z. Yang, Glucose-assisted synthesis of hierarchical flower-like Co_3O_4 nanostructures assembled by porous nanosheets for enhanced acetone sensing, *Sens. Actuators, B*, 2019, **288**, 699–706.

7 X. Qiao, C. Ma, X. Chang, X. Li, K. Li, L. Zhu, F. Xia and Q. Xue, 3D radial Co_3O_4 nanorod cluster derived from cobalt-based layered hydroxide metal salt for enhanced trace acetone detection, *Sens. Actuators, B*, 2021, **327**, 128926.

8 D. Tang, L. Jia, Z. Zhao, R. Yang, X. Wang and X. Guo, EDTA assistant preparation and gas sensing properties of Co_3O_4 nanomaterials, *J. Inorg. Mater.*, 2020, **35**, 1214–1222.

9 J. Cao, S. Wang, H. Zhang and T. Zhang, Constructing one dimensional Co_3O_4 hierarchical nanofibers as efficient sensing materials for rapid acetone gas detection, *J. Alloys Compd.*, 2019, **799**, 513–520.

10 X. Chen, S. Wang, C. Su, Y. Han, C. Zou, M. Zeng, N. Hu, Y. Su, Z. Zhou and Z. Yang, Two-dimensional Cd-doped porous Co_3O_4 nanosheets for enhanced room-temperature NO_2 sensing performance, *Sens. Actuators, B*, 2020, **305**, 127393.

11 C. Zhang, L. Li, L. Hou and W. Chen, Fabrication of Co_3O_4 nanowires assembled on the surface of hollow carbon spheres for acetone gas sensing, *Sens. Actuators, B*, 2019, **291**, 130–140.

12 K. Xu, W. Zhao, X. Yu, S. Duan and W. Zeng, MOF-derived Co_3O_4/Fe_2O_3 p–n hollow cubes for improved acetone sensing characteristics, *Phys. E*, 2020, **118**, 113869.

13 T. Akamatsu, T. Itoh, Y. Masuda, W. Shin, I. Matsubara and M. Kida, Gas sensor properties of nanopore-bearing Co_3O_4 particles containing Pt or Pd particles, *J. Asian Ceram. Soc.*, 2020, **8**, 138–148.

14 F. Qu, N. Zhang, S. Zhang, R. Zhao, D. Yao, S. Ruan and M. Yang, Construction of $Co_3O_4/CoWO_4$ core-shell urchin-like microspheres through ion-exchange method for high-performance acetone gas sensing performance, *Sens. Actuators, B*, 2020, **309**, 127711.

15 J.-S. Jang, W.-T. Koo, D.-H. Kim and I.-D. Kim, In situ coupling of multidimensional MOFs for heterogeneous metal-oxide architectures: Toward sensitive chemiresistors, *ACS Cent. Sci.*, 2018, **4**, 929–937.

16 P. Srinivasan, A. J. Kulandaisamy, G. K. Mani, K. J. Babu, K. Tsuchiya and J. B. B. Rayappan, Development of an acetone sensor using nanostructured Co_3O_4 thin films for exhaled breath analysis, *RSC Adv.*, 2019, **9**, 30226.

17 T. Zhou, T. Zhang, J. Deng, R. Zhang, Z. Lou and L. Wang, P-type Co_3O_4 nanomaterials-based gas sensor: Preparation and acetone sensing performance, *Sens. Actuators, B*, 2017, **242**, 369–377.

18 Y. Xiong, X. Chang, X. Qiao, K. Li, L. Zhu, F. Xia, X. Li, Q. Zheng, W. Xing and Q. Xue, Co-MOF-74 derived Co_3O_4/graphene heterojunction nanoscrolls for ppb-level acetone detection, *Sens. Actuators, B*, 2019, **300**, 127011.

19 Z. Yang, W. Cao, C. Peng, T. Wang, B. Li, H. Ma, Y. Su, Z. Zhou, J. Yang and M. Zeng, Construction, application and verification of a novel formaldehyde gas sensor system based on Ni-doped SnO_2 nanoparticles, *IEEE Sens. J.*, 2021, **21**, 11023–11030.

20 J. Hu, T. Wang, Y. Wang, D. Huang, G. He, Y. Han, N. Hu, Y. Su, Z. Zhou, Y. Zhang and Z. Yang, Enhanced formaldehyde detection based on Ni doping of SnO_2 nanoparticles by one-step synthesis, *Sens. Actuators, B*, 2018, **263**, 120–128.

21 J.-W. Yoon, J.-S. Kim, T.-H. Kim, Y. J. Hong, Y. C. Kang and J.-H. Lee, A new strategy for humidity independent oxide chemiresistors: Dynamic self-refreshing of In_2O_3 sensing surface assisted by layer-by-layer coated CeO_2 nanoclusters, *Small*, 2016, **12**, 4229–4240.

22 C.-H. Kwak, T.-H. Kim, S.-Y. Jeong, J.-W. Yoon, J.-S. Kim and J.-H. Lee, Humidity-independent oxide semiconductor chemiresistors using terbium-doped SnO_2 yolk-shell spheres for real-time breath analysis, *ACS Appl. Mater. Interfaces*, 2018, **10**, 18886–18894.

23 J.-S. Kim, C. W. Na, C.-H. Kwak, H.-Y. Li, J. W. Yoon, J.-H. Kim, S.-Y. Jeong and J.-H. Lee, Humidity-independent gas sensors using Pr-doped In_2O_3 macro-porous spheres: Role of cyclic Pr^{3+}/Pr^{4+} redox reactions in suppression of water poisoning effect, *ACS Appl. Mater. Interfaces*, 2019, **11**, 25322–25329.

24 H.-Y. Li, C.-S. Lee, D. H. Kim and J.-H. Lee, Flexible room-temperature NH_3 sensor for ultrasensitive, selective, and humidity-independent gas detection, *ACS Appl. Electron. Mater.*, 2018, **10**, 27858–27867.

25 X. Fan, Y. Xu, C. Ma and W. He, In-situ growth of Co_3O_4 nanoparticles based on electrospray for an acetone gas sensor, *J. Alloys Compd.*, 2021, **854**, 157234.

26 X.-X. Fan, X.-L. He, J.-P. Li, X.-G. Gao and J. Jia, Ethanol sensing properties of hierarchical SnO_2 fibers fabricated with electrospun polyvinylpyrrolidone template, *Vacuum*, 2016, **128**, 112–117.

27 F. Dang, Y. Wang, L. Xu, P. Cheng, Z. Weng, T. Wang, L. Lv, C. Wang, X. Li and B. Zhang, Solvent-dependent synthesis of okra-shaped Co_3O_4 for acetone gas detection at low operation temperatures, *ACS Appl. Electron. Mater.*, 2021, **3**, 3400–3410.

28 Y. Gao, D. Chen, X. Hou, Y. Zhang, S. Yi, H. Ji, Y. Wang, L. Yin and J. Sun, Microwave-assisted synthesis of hierarchically porous Co_3O_4/rGO nanocomposite for low-temperature acetone detection, *J. Colloid Interface Sci.*, 2021, **594**, 690–701.

29 A. Ma, S. Y. Baek, J. H. Seo, S. A. Abbas, J.-H. Kwon, S. J. Ahn and K. M. Nam, Photodeposition of Pt nanoparticles on Co_3O_4 nanocubes for detection of acetone at part-per-billion levels, *ACS Appl. Nano Mater.*, 2021, **4**, 2752–2759.

30 S. Deng, X. Liu, N. Chen, D. Deng, X. Xiao and Y. Wang, A highly sensitive VOC gas sensor using p-type mesoporous Co_3O_4 nanosheets prepared by a facile chemical coprecipitation method, *Sens. Actuators, B*, 2016, **233**, 615–623.

31 V. Amiri, H. Roshan, A. Mirzaei, G. Neri and A. I. Ayesh, Nanostructured metal oxide-based acetone gas sensors: A review, *Sensors*, 2020, **20**, 3096.

32 N. Han, G. Pan, J. Zheng, R. Wang and Y. Wang, Co_3O_4-ZnO P-N heterostructure nanomaterials film and its enhanced photoelectric response to visible lights at near room temperature, *Mater. Res.–Ibero-Am. J.*, 2019, **22**, e20180689.

33 X. Chang, X. Qiao, K. Li, P. Wang, Y. Xiong, X. Li, F. Xia and Q. Xue, UV assisted ppb-level acetone detection based on hollow ZnO/MoS_2 nanosheets core/shell heterostructures at low temperature, *Sens. Actuators, B*, 2020, **317**, 128208.